THE JOURNAL OF PHYSICAL CHEMISTRY C

Article

Cite This: J. Phys. Chem. C 2019, 123, 1444−1453

pubs.acs.org/JPCC

Effects of Zn Substitution in the Magnetic and Morphological Properties of Fe-Oxide-Based Core−Shell Nanoparticles Produced in a Single Chemical Synthesis

Javier Lohr,[†] Adriele Aparecida de Almeida,[†,‡] M. Sergio Moreno,[†] Horacio Troiani,[‡,§] Gerardo F. Goya,[∥,⊥,▽] Teobaldo Enrique Torres Molina,[⊥,▽] Rodrigo Fernandez-Pacheco,[⊥,▽] Elin L. Winkler,[†,‡] Marcelo Vasquez Mansilla,[†] Renato Cohen,[#] Luiz C. C. M. Nagamine,[#] Luis M. Rodríguez,[†] Daniel E. Fregenal,[†] Roberto D. Zysler,[†,‡] and Enio Lima, Jr.*[,†]

[†]Instituto de Nanociencia y Nanotecnología CNEA-CONICET, Centro Atómico Bariloche, Av. Bustillo 9500, 8400 San Carlos de Bariloche, Argentina

[‡]Instituto Balseiro, Universidad Nacional de Cuyo—CNEA, Av. Bustillo 9500, 8400 San Carlos de Bariloche, Argentina

[§]Laboratorio de Caracterización de Materiales y Óxidos No-Estequiometricos. Gerencia de Investigación Aplicada-CONICET-CAB, Universidad de Zaragoza, 50009 Zaragoza, Spain

[∥]Departamento de Física de la Materia Condensada, Facultad de Ciencias, Universidad de Zaragoza, 50009 Zaragoza, Spain

[⊥]Instituto de Nanociencia de Aragón (INA), Universidad de Zaragoza, 50018 Zaragoza, Spain

[▽]Laboratorio de Microscopias Avanzadas (LMA), Universidad de Zaragoza, C/Mariano Esquillor s/n, CP 50018 Zaragoza, Spain

[#]Instituto de Física, Universidade de São Paulo, 05508-090 São Paulo, Brazil

ABSTRACT: Magnetic, compositional, and morphological properties of Zn−Fe-oxide core−shell bimagnetic nanoparticles were studied for three samples with 0.00, 0.06, and 0.10 Zn/Fe ratios, as obtained from particle-induced X-ray emission analysis. The bimagnetic nanoparticles were produced in a one-step synthesis by the thermal decomposition of the respective acetylacetonates. The nanoparticles present an average particle size between 25 and 30 nm as inferred from transmission electron microscopy (TEM). High-resolution TEM images clearly show core−shell morphology for the particles in all samples. The core is composed by an antiferromagnetic (AFM) phase with a Wüstite ($Fe_{1-y}O$) structure, whereas the shell is composed by a $Zn_xFe_{3-x}O_4$ ferrimagnetic (FiM) spinel phase. Despite the low solubility of Zn in the Wüstite, electron energy-loss spectroscopy analysis indicates that Zn is distributed almost homogeneously in the whole nanoparticle. This result gives information on the formation mechanisms of the particle, indicating that the Wüstite is formed first, and the superficial oxidation results in the FiM ferrite phase with similar Zn concentration than the core. Magnetization and in-field Mössbauer spectroscopy of the Zn-richest nanoparticles indicate that the AFM phase is strongly coupled to the FiM structure of the ferrite shell, resulting in a bias field (H_{EB}) appearing below T_N^{FeO}, with H_{EB} values that depend on the core−shell relative proportion. Magnetic characterization also indicates a strong magnetic frustration for the samples with higher Zn concentration, even at low temperatures.

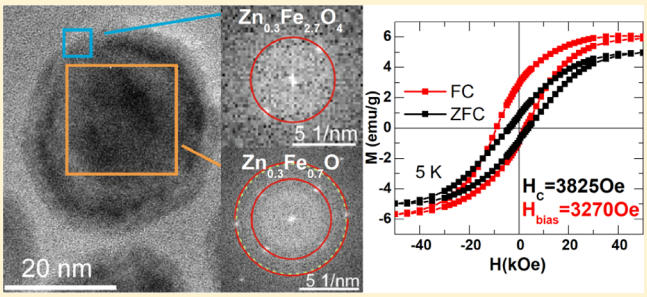

INTRODUCTION

In the early 2000s, the groups of Sun[1,2] and Hyeon[3,4] reported the synthesis of magnetic ferrite nanoparticles by thermal decomposition at relatively high temperatures (about 540−640 K) of organometallic precursors in the presence of surfactants and a long-chain alcohol. This method becomes a hit because it produces magnetic nanoparticles with several advantages with respect to others,[5] such as a narrow size distribution and a high crystallinity, both critical for homogeneous magnetic properties, and simultaneously, it allows an easy way to control stoichiometry.[2] The success of this method is based in a well separately nucleation and growth/crystallization process that takes place at different temperatures,[6] being extensively used to synthesize magnetic nanoparticles.[7−12]

An interesting feature was reported on the fundamentals of the thermal decomposition method by Hou et al. in 2007:[13] a massive reduction of iron ions in the synthesis solution, leading to the formation of nanoparticles with a diameter larger than 14 nm containing the antiferromagnetic (AFM) Wüstite phase ($Fe_{1-y}O$), which is followed by the oxidation and consequent

Received: September 13, 2018
Revised: December 18, 2018
Published: December 20, 2018

DOI: 10.1021/acs.jpcc.8b08988
J. Phys. Chem. C 2019, 123, 1444−1453

formation of a ferrimagnetic (FiM) ferrite phase (Fe_3O_4 or γ-Fe_2O_3). The result was a bimagnetic core−shell nanoparticle produced in a one-pot reaction, with an AFM core ($Fe_{1-y}O$) below T_N = 198 K[14] and a FiM shell. In fact, in the work of Hyeon et al. in 2004,[3] it was possible to observe remarkable features around 200 K in the zero-field cooling (ZFC) magnetization versus temperature curves for large particles (d > 16 nm) that could be related to the Néel temperature (T_N) of the AFM phase. When the formation of the $Fe_{1-y}O$ phase took place during the synthesis, the presence of the AFM phase is expected for larger particles because the oxidation to the FiM phase could not be complete, with an AFM core. Other works report on the formation of $Fe_{1-y}O$ and a ferrite phase in a core−shell structure after oxidation by the thermal decomposition method.[15−19] As pointed out by Chen et al.,[20] the Wüstite phase is formed as a consequence of reactions involving some commonly used hydrocarbon solvents and its formation contributes to a significant cationic disorder. The latter formation of the bimagnetic core−shell system due to the surface oxidation of Wüstite results in very distinct magnetic properties with respect to the monophasic nanoparticles.[21−26] Therefore, it is very important to determine the factors that govern the formation of core−shell nanoparticles to establish the reproducibility of this synthesis method and the magnetic response of the system. Different magnetic ions present different degrees of solubility in the Wüstite phase. While Chen et al.[27] have determined a relatively homogeneous distribution of Co ions along the entire particle, including the core (Wüstite) and shell (ferrite), and similar observation was found for the Mn ions[28] and also for the diamagnetic Mg^{2+} ion,[29−31] the Zn^{2+} ions present low solubility in the Wüstite with an upper limit of approximately 10%.[32] This result can lead to a stoichiometric heterogeneity when the formation of $Fe_{1-y}O$ takes place with important consequences in the magnetic response of the system. As the production of iron oxide nanoparticles doped with Zn is of great current interest because of the surface chemistry of the system as well as its magnetic response for bioapplication and innovative technologies,[33−36] it is crucial to determine the role of the different parameter that establishes the morphology and magnetic properties of this system. With this premise, in this work, we have produced Zn−$Fe_{1-y}O$/$Zn_xFe_{3-x}O_4$ bimagnetic core−shell nanoparticles by the thermal decomposition method and studied their structural, morphology, and magnetic properties. We have analyzed the effect of the low solubility of Zn in the Wüstite in the composition homogeneity and its effects on the physical properties of the nanoparticles.

EXPERIMENTAL PROCEDURE

Sample Preparation. Three samples with distinct Zn amounts in the composition were prepared by the thermal decomposition of Fe^{3+} acetylacetonate ($Fe(C_5H_7O_2)_3$—Fe(acac)$_3$—Aldrich 97%) and Zn^{2+} acetylacetonate [Zn$(C_5H_7O_2)_2{\cdot}xH_2O$—Zn(acac)$_2$—Aldrich, with estimation of 20% wt of water as obtained from differential thermal analysis−thermogravimetric analysis (TGA) measurements]. Samples were labeled according to the Zn/Fe relation determined by particle-induced X-ray emission (PIXE) analysis (z = $[Zn]_{PIXE}/[Fe]_{PIXE}$): z = 0.10, z = 0.06, z = 0.00. For sample z = 0.00, a total of 5.7 mM Fe(acac)$_3$ were dispersed in 50 mL of octadecene ($CH_3(CH_2)_{15}CH{=}CH_2$—Aldrich 90%) with 56.6 mM oleic acid ($CH_3(CH_2)_7CH{=}CH(CH_2)_7COOH$—PanReac, PharmaGrade), 56.6 mM oleylamine ($CH_3(CH_2)_7CH{=}CH(CH_2)_7CH_2NH_2$—Aldrich 70%), and 5.7 mM 1,2-octanediol ($CH_3(CH_2)_5CH(OH)$-CH_2OH—Aldrich 98%). Sample z = 0.06 was prepared with 4.5 mM Fe(acac)$_3$ and 0.5 mM Zn(acac)$_2$ dispersed in 50 mL of octadecene and with the addition of 26 mM oleic acid, 26 mM oleylamine, and 3.5 mM 1,2-octanediol. Sample z = 0.10 was prepared using 4.6 mM Fe(acac)$_3$ and 1.1 mM Zn(acac)$_2$ dispersed in 50 mL of trioctylamine ($[CH_3(CH_2)_7]_3N$—Aldrich 98%) and 22.5 mM oleic acid. For all samples, a three-necked flask was used with the first neck for the N_2 (White Martins—5.0) flux, the second for mechanical stirring (the central one), and the third one for a condenser. The synthesis solution of all samples was mechanically stirred at room temperature and heated to 373−393 K for 30 min with a N_2 flux of 0.5 mL/min, without the presence of a condenser in order to remove the humidity of the system. After that, the system was closed with the condenser keeping the N_2 flux, and the solution was heated up to 473 K with a controlled increment of temperature (about 3 K/min.). The solution was kept in this temperature for about 5 min, and then it was heated up to the reflux condition with a heating ramp of ∼20 K/min: 610−615 K for octadecene and 630−635 K for trioctylamine. After that, the heating source was removed in order to get a rapid cooling of the solution. At 313 K, the flask was opened, and 400 mL of ethanol (96%—Porta) was added in order to precipitate the particles. Finally, a solution of ethanol and acetone (99.9%—Sigma-Aldrich) (about 10:1, respectively) was added to further precipitate the particles, followed by centrifugation at 14000 rpm for 30 min. A second cleaning is also done only with acetone, followed by centrifugation. The final product, the as-made sample, is a powder containing hydrophobic nanoparticles coated with an organic layer of oleic acid.

A differential thermal TGA Shimadzu DTG-60H was used to determinate the percentage of the organic compound in the as-made nanoparticles to have accuracy in the mass determination to normalize the magnetization experimental data with the oxide amount. For this, each as-made powder sample was heated up to 1173 K with a heating rate of 3 K/min in the Ar flux (100 mL/min), whereas the weight loss was measured, which corresponds to the amount of the organic compound in nanoparticles. This technique was also used to determine the amount of water in Zn(acac)$_2$, where the reagent was heated up to 453 K with a heating rate of 3 K/min in the Ar flux (100 mL/min).

Structural characterization was carried out using a PANalytical Empyrean powder X-ray diffractometer (Cu Kα, λ = 0.15418 nm). Samples were cleaned with acetone to remove the organic material, and a zero diffraction plate holder was used in the measurement.

Transmission electron microscopy (TEM) images were recorded in two microscopes. For both microscopes, TEM specimens were prepared by dispersing the dried powdered samples in isopropanol and dropping the solution onto a carbon-covered grid. For TEM and high-resolution TEM (HRTEM), the images were obtained with a Tecnai F20 G2 (ThermoFisher Scientific, formerly FEI) microscope operating at 200 kV at room temperature. The mean particle size ($\langle D \rangle$) was determined after a count of ∼300 particles and fitting the corresponding histogram with a lognormal distribution. For the scanning TEM−high-angle annular dark field (STEM−HAADF), the images were obtained in a Cs-probe-corrected Titan (ThermoFisher Scientific, formerly FEI) at a working

DOI: 10.1021/acs.jpcc.8b08988
J. Phys. Chem. C 2019, 123, 1444−1453

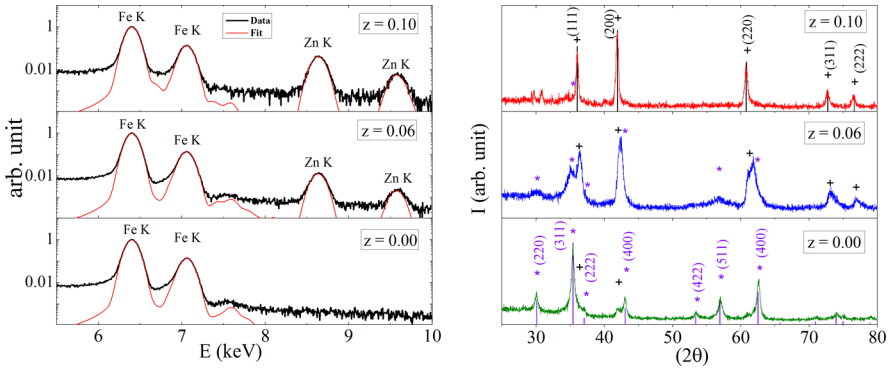

Figure 1. Left panel: PIXE spectra of all samples showing the pertinent energy range of Fe and Zn K-peaks. Black lines correspond to experimental data, and red lines are the respective fitting to obtain the z = [Zn]/[Fe] ratio for each system. Right panel: XRD profiles of three samples. All peaks are indexed with the $Fe_{1-y}O$ (+) and ferrite (*) phases where the bars correspond to the diffraction peaks according to the JCPDS card number: for Wüstite 00-006-0615 (upper panel) and magnetite 00-019-0629 (bottom panel).

Table 1. Nanoparticle Characteristics Obtained from TEM, $M(T)$, and $M(H)$ measurements: % V_{shell} is the Volume Percentage of the Shell As Calculated from the Shell Thickness and Core Diameter from TEM Images, M_S Is the Saturation Magnetization at Room Temperature, T_N Is the Néel Temperature, H_{bias}^{5K} and H_{bias}^{100K} Are the Exchange Bias Fields, and H_C^{5K} and H_C^{100K} Are the Coercive Fields, Obtained from $M_{FC}(H)$ Curves at 5 and 100 K, Respectively

sample	% V_{shell} (%)	M_S (emu/g)	T_N (K)	H_{bias}^{5K} (Oe)	H_C^{5K} (Oe)	H_{bias}^{100K} (Oe)	H_C^{100K} (Oe)
z = 0.00	70	59.6	196	86	30	30	454
z = 0.06 (2)	65	16.8	180	2270	3580	435	673
z = 0.10 (2)	55	3.2	177	3420	6150	429	276

voltage of 300 kV, coupled with a HAADF detector (Fischione). The chemical composition of the nanoparticles was analyzed by electron energy-loss spectroscopy (EELS), in order to obtain the concentration ratio of Fe/Zn at the core and the shell. Low-loss EEL spectra were obtained with a Tridiem Energy Filter (Gatan) spectrometer. For every line scan, a 5 ms spectrum was obtained every 0.1 nm. The energy dispersion used for the analysis was 0.1 eV/pixel. The collection semiangle (Beta) was 32.6 mrad for a camera length of 10 mm and a spectrometer entrance aperture of 1 μm. The convergence semiangle (Alpha) was 24.8 mrad for a condenser aperture of 70 μm. The energy resolution, estimated from the full width at half-maximum (fwhm) of the zero-loss peak, was 1.4 eV.

The chemical composition of the nanoparticles was measured with the PIXE spectroscopy technique,[37] with a 3 MeV H^+ beam in a NEC 5SDH 1.7 MV tandem accelerator with a NEC RC43 end-station.[38] To prepare the nanoparticle samples, they were properly washed and dried and then placed on the sample holder with a carbon tape. PIXE spectra were analyzed using GUPIX software.[39]

Magnetization measurements as a function of temperature ($M(T)$) and isothermal curves (T = 5 K) as a function of the applied field ($M_{5K}(H)$) were measured in a commercial Quantum Design MPMS-5S SQUID magnetometer. $M(T)$ curves were measured with an applied field of 50 Oe in ZFC and field cooling (FC) protocols. $M_{5K}(H)$ curves were measured in both conditions: after ZFC protocol and after a FC protocol. For the FC protocol, the sample was cooled from T = 300 to 5 K (starting above the $T_N \approx$ 200 K of the $Fe_{1-y}O$ AFM phase) with an applied field of H_{FC} = 50 kOe. Isothermal curves at T = 100 K ($M_{100K}(H)$) and 300 K ($M_{300K}(H)$) were measured in a LakeShore 7300 vibrating sample magnetometer. $M_{100K}(H)$ measurements were also performed in both ZFC and FC protocols, with an applied field in the cooling procedure of H_{FC} = 10 kOe. $M_{300K}(H)$ measurements were used in order to determine saturation magnetization (M_S) at room temperature. For all magnetic measurements, the samples were conditioned by dispersing the nanoparticles in toluene and paraffin, followed by the toluene evaporation, in order to avoid agglomeration and to immobilize them.

In-field Mössbauer spectra (MS) of sample z = 0.10 were taken at 4.2 K in a liquid He flow cryostat with a spectrometer in transmission geometry with a ^{57}Co/Rh source. The spectra were collected after a FC procedure with an applied field of H_{FC} = 120 kOe from 300 K (above T_N). Mössbauer samples were prepared by dispersing 20 mg of the respective powder samples in boron nitride and by pressing it between acrylic disks. The sample was mounted in the bore of a 140 kOe superconducting magnet in a vertical source-sample-detector setup such that the direction of gamma ray was parallel to the direction of the applied field. A sine-shaped velocity waveform was used to minimize the mechanical noise. All MS spectra were fitted by using Lorentzian line shapes with nonlinear least-square software by calibrating the velocity scale with α-Fe foil at 300 K. Isomer shift (IS) values are relative to α-Fe at 300 K. As a consequence of the experimental setup, the temperature of the source during the low-temperature spectrum acquisition must be considered as an important factor to the IS values observed in order to compare with the expected ones.

RESULTS AND DISCUSSION

Morphology and Composition. Figure 1 shows the measured PIXE spectra of all as-made samples and their corresponding fittings performed with GUPIX software. The procedure of fabrication and sample preparation involves the presence of extra elements, mainly carbon and oxygen because of the imponderable contribution from different sources, such as carbon tape, solvent remains, and contamination. Restricting

DOI: 10.1021/acs.jpcc.8b08988
J. Phys. Chem. C 2019, 123, 1444−1453

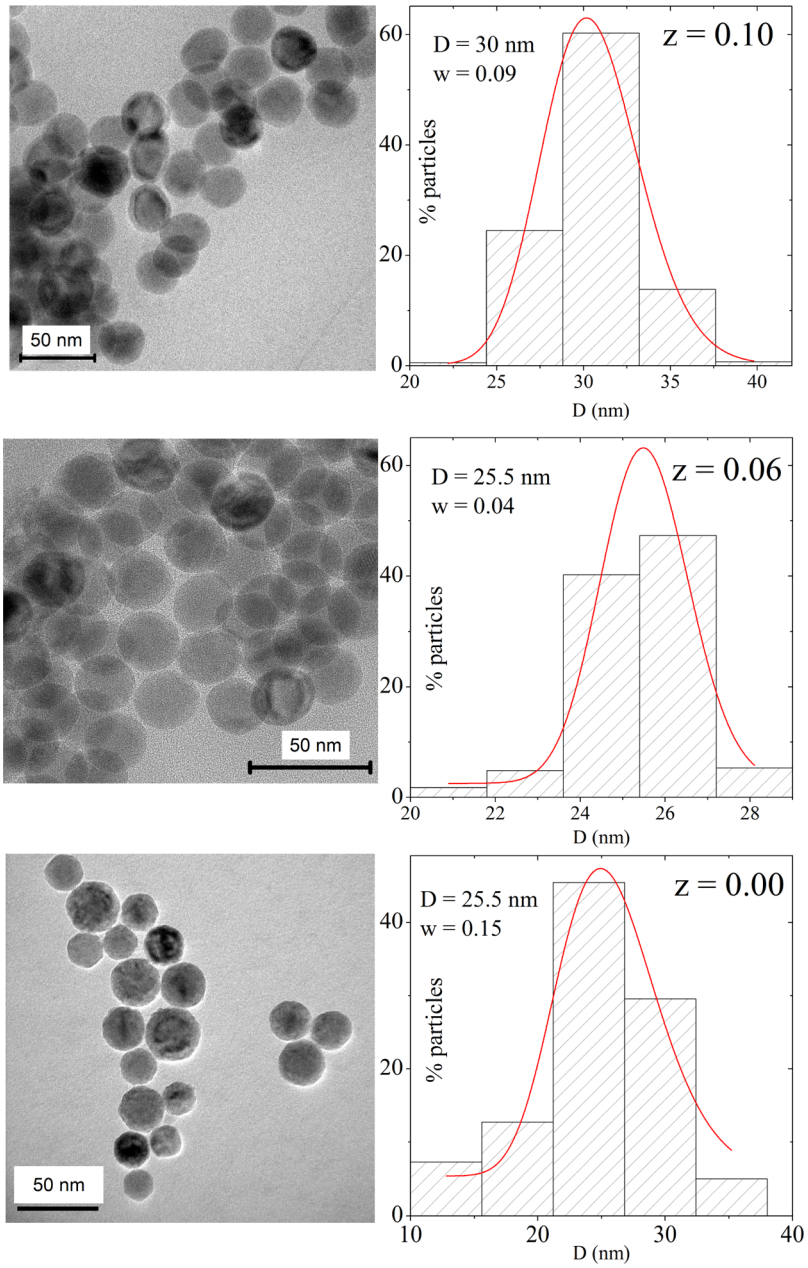

Figure 2. Representative TEM image for each sample with the corresponding histogram of diameters obtained with measuring more than 300 particles. Each histogram is fitted with a lognormal distribution in order to obtain the mean diameter and dispersion.

us to the nanoparticle composition, just the Zn and Fe quantities are taken into account using the peaks associated with the K-shell transitions. The value $z = [Zn]_{PIXE}/[Fe]_{PIXE}$ for each sample was used to label each sample in Table 1, with the corresponding uncertainty in the parenthesis. The amount of Zn in samples z = 0.10 (2) and 0.06 (2) is lower than the expected from the molar relation of precursors ($[Zn(acac)_2]/[Fe(acac)_3]$) used in the synthesis procedure: 0.58 for sample z = 0.10 (2) and 0.30 for sample z = 0.06 (2). This result indicates that the incorporation of the Zn ions to the nanoparticles is limited in the synthesis procedure, probably as a consequence of the low Zn solubility in the Wüstite phase.

Figure 1 also presents the X-ray diffraction (XRD) patterns of samples z = 0.10, 0.06, and 0.00. The diffraction pattern of the sample with z = 0.10 mainly corresponds to the phase $Fe_{1-y}O$, although some peaks of ferrite phase are observed with very low intensity. The peaks (111), (200), and (220) of $Fe_{1-y}O$ were fitted with a pseudo-Voigt function in order to obtain the fwhm, and then the crystallite size (D_{XRD}) was obtained by using the Scherrer equation, which results in the 20−25 nm range. Instead, the XRD profile of sample z = 0.06 clearly evidences the presence of a ferrite structure together with the $Fe_{1-y}O$ phase, in almost similar amounts when considering the peak areas. From the Scherrer equation, the D_{XRD} was calculated for these phases, obtaining 7 nm for the reflection (311) of the ferrite phase and 15 nm for the reflection (111) of the $Fe_{1-y}O$ phase. Moreover, for sample z = 0.00, both phases are also observed, with a relation of ferrite/$Fe_{1-y}O$ ≈ 2/1 obtained from the respective peak area. The values of D_{XRD} ≈ 12 and 21 nm were calculated from the reflection (200) of the $Fe_{1-y}O$ phase and from the reflections (311) and (400) of the ferrite, respectively. The XRD analysis

DOI: 10.1021/acs.jpcc.8b08988
J. Phys. Chem. C 2019, 123, 1444−1453

of the three samples shows that the proportion of the Wüstite phase increases as the Zn concentration in the particles increases: from a predominant ferrite phase for sample $z = 0.00$ to the widely dominant Wüstite phase in sample $z = 0.10$, in concordance with the increment in the corresponding crystallite size D_{XRD} of this phase.

Figure 2 shows representative TEM images at the lower magnification of the nanoparticles in samples $z = 0.10$, 0.06, and 0.00. The diameter histogram for each sample was constructed by measuring the diameter of more than 300 nanoparticles, also presented in Figure 2. The histograms were fitted with a lognormal distribution, and the mean diameters are 30, 26, and 26 nm for samples $z = 0.10$, 0.06, and 0.00, respectively, with a dispersion of $\sigma \approx 0.2$ nm. A core−shell structure is observed in TEM images even at low magnification. From TEM images at higher magnification, the shell thickness was measured and the relative volume of each component was calculated, obtaining the volume proportion for the shell (% V_{shell}) of 55% for sample $z = 0.10$, 65% for $z = 0.06$, and 70% for $z = 0.00$, as given in Table 1. Figure 3a shows a representative HRTEM image of the nanoparticle in $z = 0.10$, where the core−shell is clearly evidenced. The fast Fourier transform (FFT) of different zones

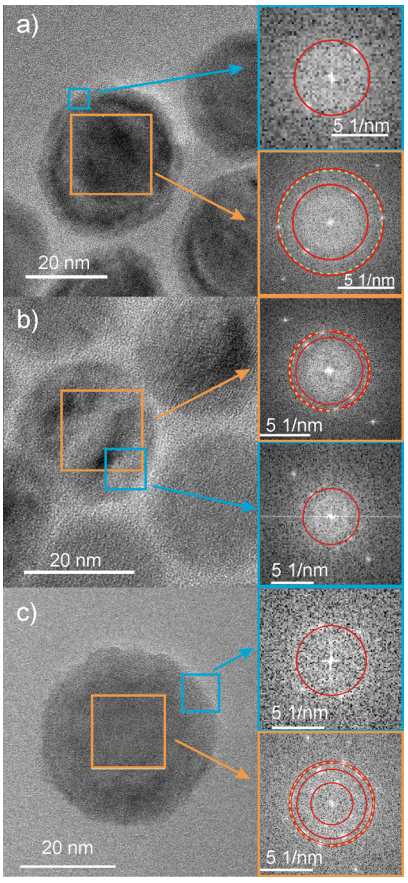

Figure 3. Left panels show the HRTEM image of a representative nanoparticle of the sample with $z = 0.10$ (a), $z = 0.06$ (b), and $z = 0.00$ (c); right panels show the FFT from the zones marked with a square in the HRTEM image of the core (green) and shell (blue), as indicated by the arrows. The FFT patterns of the shell were indexed with the cubic spinel interplanar distances (solid red line), whereas the patterns of the core are indexed with cubic spinel and Wüstite (orange dashed line) interplanar distances.

in the same particle gives the reciprocal d-spacing of each morphological component (core and shell). The FFT (upper right panel) of the shell zone (light blue square in HRTEM) shows exclusively a d-spacing corresponding to the plane (220) of ferrite, which is marked as a red solid line circle; any contribution of Wüstite is not expected in this d-spacing range. Other interplanar distances appear for a large zone inside the core (orange square in HRTEM): the reciprocal distances observed in this FFT image between the planes (220) and (400) of ferrite correspond to a d-spacing corresponding to the plane (200) of Wüstite, which is indicated in the figure as the green dashed line. Similar characteristics are observed for the HRTEM of $z = 0.06$ (Figure 3b). The FFT of the shell zone also shows spots corresponding to the (220) plane of ferrite (marked in figure as a red solid line), whereas the FFT of a large area with the core and shell of the particles presents other distances: the red circles for (311) and (222) of ferrite and green dashed line circle for (111) of the Wüstite phase. Finally, similar results are also obtained from the HRTEM of $z = 0.00$ (Figure 3c). The FFT in the shell zone shows spots corresponding to the (220) plane of ferrites (red online) and the FFT of the core shows family of planes: (111), (220), (311), and (222) (not marked in the figure) for ferrites and the reciprocal interplanar distance for (111) of Wüstite. Our result shows that sample $z = 0.10$ has a bigger core volume than the other samples, presenting a systematic increase of % V_{shell} with the Zn amount. Nevertheless, its increment in the core volume with the amount of Zn not necessarily can be an exclusive consequence of the amount of Zn in the sample or in the synthesis solution. Other small changes in the synthesis conditions, including the redox potential, could be related to this change.

Figure 4 shows a representative STEM−HAADF image of the nanoparticles (left panel) corresponding to the sample with $z = 0.10$. The line scan used for STEM SI is indicated. Two spectra corresponding to the shell and the center of the core were extracted at the positions indicated in the image and shown in the right panel. In the spectra, the Fe−M edges are visible at about 60 eV. The Zn−M edges can be observed as a weak bump at about 84 eV. For the extraction of these edges, an AE^{-r} power law background was subtracted. The width of the energy window for typical background fit for the Zn edge and the estimated background are indicated in Figure 4. The background-subtracted Zn−M edges are shown. The Fe/Zn ratio obtained at both positions was the same for the range 8−9. This evaluation indicates that Zn is present over the whole volume of the nanoparticle and that the doping concentration is approximately the same in the core and in the shell.

Considering the morphological and compositional analyses, we can obtain information about the growth mechanisms of the core−shell nanostructures. These results are consistent with the formation of $Fe_{1-y}O$, at the initial stage of the synthesis, followed by the formation of the ferrite phase as a consequence of the surface oxidation, which are in agreement with the PIXE analysis. This growth mechanism leads to the formation of well-defined interfaces, when they are compared with systems where the shell is grown in a second reaction,[22,40] with the expectation of an improved magnetic exchange interaction between the phases. Other interesting feature is the reduction in the Zn incorporation in the formed material related to the nominal composition, which is probably related with the well-known low solubility of Zn in the Wüstite structure mentioned before.[32]

DOI: 10.1021/acs.jpcc.8b08988
J. Phys. Chem. C 2019, 123, 1444−1453

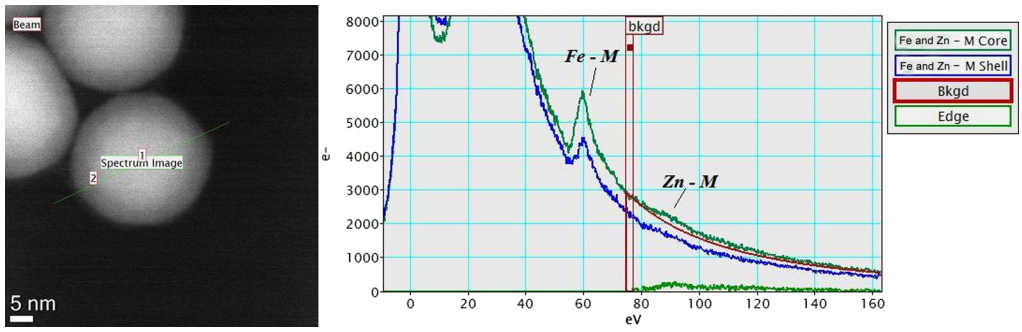

Figure 4. STEM−HAADF image of nanoparticles of sample z = 0.10 (left) and low-loss EEL spectra (right) at different positions of the nanoparticle (indicated by 1 and 2 in the figure). The Fe−M and Zn−M edges are indicated. The background subtracted is indicated (red line). The background-subtracted Zn−M edge is also shown.

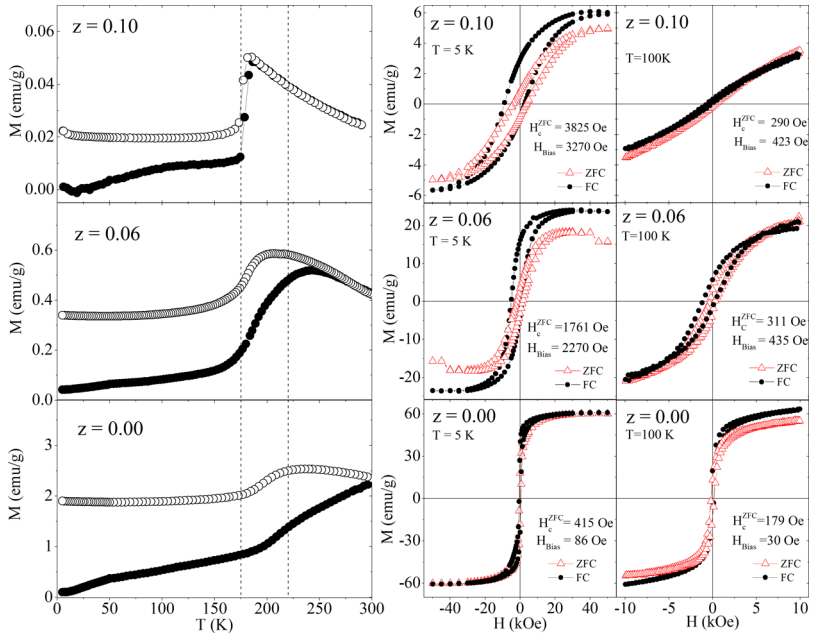

Figure 5. Left panel: $M(T)$ data of all samples measured in both ZFC (solid symbols) and FC (open symbols) protocols with H_{FC} = 50 Oe. Right panel: ZFC (open symbols) and FC (solid symbols) hysteresis loops measured at 5 K (left panels) and 100 K (right panels). The values of coercive fields after ZFC (H_C^{ZFC}) and bias fields after FC defined as $H_{bias} = (H_C^+ - H_C^-)/2$) are also displayed.

Magnetic Properties. $M(T)$ curves of all samples measured in ZFC and FC protocols with H = 50 Oe are presented in Figure 5. The characteristic FC magnetization curves of nanoparticles of the FiM material below the blocking temperature are a slightly increasing curve with a not so pronounced slope.[41] For our samples, a marked decrease in the magnetization in 175 K < T < 210 K is observed for both ZFC and FC curves for all samples. This decrease is associated with the AFM ordering transition at the Néel temperature, of the Wüstite phase (T_N values of all samples are presented in Table 1). For this range of composition, the AFM transition temperature does not show a significant dependence with the Zn concentration. It is noteworthy that the decrease in the magnetization at T_N is larger with an increase in the Zn content, in concordance with the increasing proportion of the AFM Wüstite phase as revealed by the XRD and TEM analyses. Notice that for sample z = 0.10, where the Wüstite is the main phase, a sharper AFM transition at T_N is observed. Interestingly, irreversibility between ZFC and FC curves is observed below T_N. This irreversibility is ascribed to the magnetic behavior of the shell FiM phase, which is strongly magnetically coupled to the AFM core below T_N. Therefore, as expected for the strongly FiM-soft/AFM-hard exchange coupled system, the blocking temperature shifts to the Néel temperature of the hard magnetic component.[21,23] Instead, for samples with z = 0.06 and z = 0.00, the irreversibility temperature is above T_N, indicating that there is a distribution of nanoparticles with blocking temperatures above T_N. This result could be the consequence of the larger proportion of the FiM spinel shell phase as determined by TEM and XRD measurements and also of the lower concentration of Zn in the shell, which lead to an increase of the shell magnetic anisotropy. As a consequence, the AFM transition in these samples is smoothed in comparison to that of sample z = 0.10.

The saturation magnetization of the samples was determined from the $M(H)$ curves measured at T = 300 K. As observed in Table 1, M_S decreases from 60 to 3 emu/g when the concentration of Zn increases. The huge reduction in M_S for sample z = 0.10 comes mainly from the larger proportion of the Wüstite phase, which is paramagnetic at room temperature. Besides, the larger substitution of Fe by Zn, plus the surface disorder driven by the thinner shell in this sample, could

DOI: 10.1021/acs.jpcc.8b08988
J. Phys. Chem. C 2019, 123, 1444−1453

induce a strong spin canting in the FiM shell, which reduces M_S and the effective magnetic anisotropy K.[42]

The zinc ferrite normal spinel shows AFM ordering below ~10 K; instead, in our partially substituted ferrite, FiM ordering is expected.[43,44] Although Zn^{2+} has tetrahedral site preference in the spinel structure, at nanometric scale some cationic inversion degree is observed. It is also well-known that the presence of Zn leads to spin canting as a result of its diamagnetic nature and the consequent lack of exchange coupling for Fe^{3+} and Fe^{2+} in the neighborhood for Zn concentrations higher than 0.16.[45] In addition, spin canting is observed for systems as the only consequence of the nanometric size,[43,44] which should be increased in our system as a consequence of the thickness of the ferrite phase shell estimated of 5 nm for sample z = 0.10. Finally, a strong magnetic interaction between the FiM shell and the AFM core leads to the increment of uncompensated spins from the core and/or shell as well as to the increment of the magnetic canting in the shell phase.[21,46] Thus, the low magnetization values for high fields observed for sample z = 0.10 probably reflect the nanometric core−shell magnetically coupled nature of the nanoparticles together with the partial substitution of the Fe ion by Zn ions in the shell.

The hysteresis curves at T = 5 K and T = 100 K were measured by using two different protocols (Figure 5 right panel): after cooling from 300 K without (ZFC) and with an applied magnetic field of 50 kOe (FC). Remarkably, in the FC mode, all samples shows large exchange bias fields (H_{bias}). The presence of H_{bias} indicates a strong magnetic coupling between the AFM and the FiM phases, supporting the same conclusion observed in $M(T)$ curves where an increases of the blocking temperature of the shell to the AFM ordering transition temperature of the core was observed. Sample z = 0.10 presents the larger exchange bias field where at 5 K $H_{bias}{}^{5K} \approx$ 3420 Oe is resulted. However, the FC cycle measured up to 5 T corresponds to a minor cycle, and larger $H_{bias}{}^{5K}$ is expected for higher applied fields. Sample z = 0.06 presents a totally saturated magnetization loop at 5 K; besides, the M_S and the H_C measured from the FC cycle are larger than the ones obtained from the ZFC measurement. This result is a consequence of the magnetic coupling at the AFM/FiM interface, where the FC protocol preferentially orients the AFM surface spins, and as a consequence, it enhances the coercivity and also the saturation magnetization. As expected, the sample with z = 0.00 presents the lower $H_{bias}{}^{5K}$ (86 Oe) and the largest value of M_S because it has the smallest AFM phase proportion.

Although in an ideal AFM/FiM exchange coupled system it is predicted that the exchange bias properties should be present up to T_N, in core−shell nanoparticles, as a consequence of finite size effect and surface imperfections, it is usually observed that the exchange bias field vanishes at much lower temperature.[22] In the present system, the measurements performed at 100 K also present exchange bias field ($H_{bias}{}^{100K}$), indicating a good magnetic coupling through the interface; in fact, the exchange bias was observed up to 150 K for sample z = 0.10, close to the ordering temperature of the AFM phase. Figure 6 compares the variation of $H_{bias}{}^{5K}$ and $H_{bias}{}^{100K}$ with the Zn concentration. As expected, $H_{bias}{}^{5K}$ and also $H_C{}^{5K}$ increase with the Zn amount because the diameter of the AFM core grows, and consequently, the magnetic anisotropy of the AFM phase increases relatively to the other concentration. Instead, at

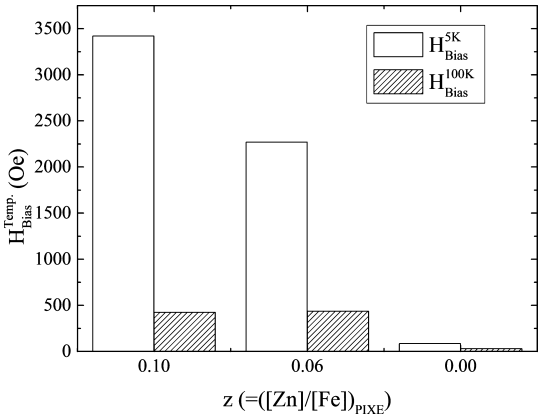

Figure 6. Exchange bias field at 5 K ($H_{bias}{}^{5K}$) and 100 K ($H_{bias}{}^{100K}$) as a function of the Zn concentration of the sample obtained from PIXE analysis.

higher temperature, $H_{bias}{}^{100K}$ and $H_C{}^{100K}$ do not follow a monotonous dependence with the concentration. We ascribed this behavior to the thermal fluctuations, which are more important when the anisotropy is reduced as a consequence of the Zn incorporation in the structure. In summary, the overall magnetic measurements indicate that the nanoparticle cores are composed by the AFM phase with a Wüstite structure, whereas the shell presents a FiM ordering, both phases are strongly coupled below T_N even at temperature higher than 100 K, and finally, the properties of the ferrite phase in the shell differ from those of magnetite or maghemite as a consequence of the coupling and the surface disorder.

In-Field Mössbauer Spectroscopy. In order to get local information about the magnetic arrangement with the presence of Zn in the bimagnetic core−shell structure, in-field Mössbauer spectroscopy was performed for sample z = 0.10. The spectra are given in Figure 7, and they were collected with different applied fields. The spectra were fitted with two crystalline sextets, labeled sextets 1 and 2, a singlet probably related to Fe^{3+} ions in the tetrahedral interstitial sites of the Wüstite structure[18,47,48] and sextet with broad lines and lower effective field ($\vec{B}_{eff} = \vec{B}_{hyp} + \vec{B}_{app}$, and $\vec{B}_{hyp}$ is the hyperfine field), labeled sextet 3. The line width was hold between the widths of the six lines of sextet: $\Gamma_{3,4} = W + 0.02526 \times dW$, $\Gamma_{2,5} = W + 0.09344 \times dW$, $\Gamma_{1,6} = W + 0.16147 \times dW$. This can be shown to result from a relatively narrow effective field distribution, such as can often be seen in ferrites. All hyperfine parameters obtained from the fitting procedure are given in Table 2. For the applied field from 0 to 120 kOe, the hyperfine field of the sextets 1 and 2, those with larger B_{eff} increase and decrease, respectively, with the applied field as expected for a strong AFM alignment, specifically for a FiM ordering as the subspectra areas are different with a relative relation of 1:1.6. These sextets could be easily referred to the two AFM aligned magnetic sublattices of the ferrite[49,50] consistent with the absence of the Verwey transition and in an opposition to the five sextets of the magnetite below the Verwey transition.[47] Nevertheless, as the Zn ions are known to occupy preferentially the A site in the ferrite structure, we expect an increase in this relation from 1.67 or 2 (maghemite or magnetite), not the observed decrease. In another way, if we consider a strong coupling among both sites, with the AFM ordering in the phase with the structure of Wüstite aligned with the A and B magnetic lattices of the ferrite, and

DOI: 10.1021/acs.jpcc.8b08988
J. Phys. Chem. C 2019, 123, 1444−1453

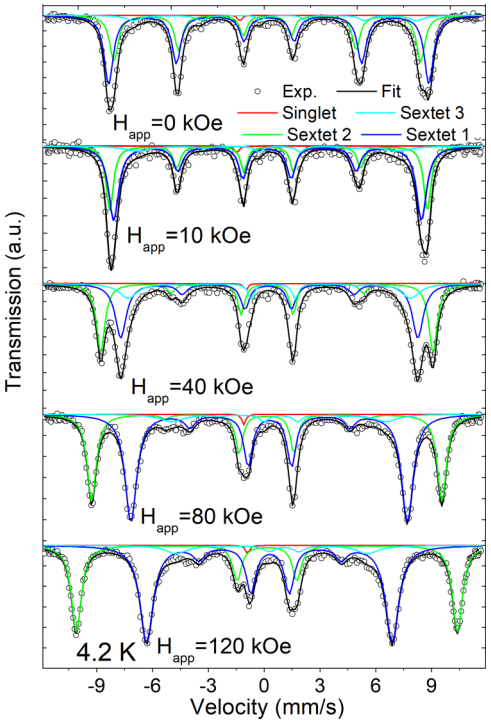

Figure 7. In-field Mossbauer spectra of sample z = 0.10 collected at 4.2 K with an applied field up to 120 kOe. All the spectra were fitted with three sextets (sextet 1—blue, sextet 2—green, and sextet 3—light blue) and a singlet (red).

considering the presence of 10% of Zn in the A site of the ferrite structure and the amounts of each phase as obtained from the volume estimated from HRTEM images, then a relation of areas about 1.60 between both sites is expected, very similar to that obtained from the fitting procedure. In this way, our in-field Mössbauer data probably indicate a strong correlation among the magnetic phases, with the sublattices of ferrite and those of AFM phase being strongly coupled and mostly aligned parallel and antiparallel to the applied field direction. Another interesting feature concerning the dependence of the B_{eff} of these sites with the applied field is observed, with a nonlinear dependence. Specifically, for H_{app} < 120 kOe, both sextets present a linear dependence but with an angular coefficient of 0.8, lower than the expected for a perfect alignment (about 1), with B_{eff} at H_{app} = 120 kOe being the expected for a perfect alignment. Therefore, this effect probably indicates a canting of these lattices probably related to a spin-glass-like in the AFM phase or in the interface layer of the core−shell nanostructure.[44] Moreover, the angles between the Fe magnetic moment and the external magnetic field (θ, displayed in Table 2) can be calculated from the D12 parameter,[50] and these angles corroborate with this argument. The third sextet with lower area and B_{eff} is probably also related to a spin-glass-like magnetic structure in the AFM phase or in the interface between the magnetic phases.

CONCLUSIONS

The synthesis of Zn-incorporated iron-oxide core−shell bimagnetic nanoparticles presented in this work represents a novel approach to the control of their magnetic properties by a chemically tunable, magnetically coupled FiM shell. The formation of an AFM $Fe_{1-y}O$ core strongly coupled to the FiM ferrite shell can be simply obtained from a standard one-pot thermal decomposition synthesis from $Fe(acac)_3$ and $Zn(acac)_2$ precursors. Compositional analysis by PIXE indicates that the Zn incorporation in the particle is lower than the nominal value of the synthesis; at the same time, the compositional analysis by EELS indicates that Zn is incorporated almost homogeneously in the whole particle, including the core and the shell. This result is interesting

Table 2. Hyperfine Parameters Obtained from the Fitting Procedure of the In-Field Mössbuer Spectra at 4.2 K: H_{app} Is the Applied Field, B_{eff} Is the Effective Field, IS Is the Isomer Shift, QS Is the Quadrupolar Splitting, W Is the Line Width, dW Is a Parameter Related with the Width of Each Line of the Sextets, D21 Is the Relation between the Intensities of the Lines 1 and 2, and the Area Is the Relative Absorption Area of Each Component

H_{app} (kOe)	subspectra	B_{eff} (T)	IS (mm/s)	QS (mm/s)	W (mm/s)	dW	D21	θ degree	area (%)
120	sextet 1	63.4	0.28	−0.01	0.55	0.59	0	0	35.4
	sextet 2	40.9	0.43	−0.04	0.60	1.60	0.12	156	56.7
	singlet		−0.89		0.23				0.5
	sextet 3	31.8	0.87	−0.64	0.59	5.00	0	0	7.4
80	sextet 1	58.3	0.27	0.01	0.44	0.93	0.04	14	35.1
	sextet 2	46.0	0.42	−0.04	0.52	1.39	0.10	158	56.2
	singlet		−0.97		0.23				0.6
	sextet 3	35.7	0.97	−0.11	0.38	7.07	0.12	24	8.1
40	sextet 1	55.3	0.29	−0.02	0.41	0.81	0.12	24	30.5
	sextet 2	49.4	0.38	0.06	0.53	1.19	0.17	152	48.9
	singlet		−0.85		0.23				0.6
	sextet 3	47.0	0.51	−0.21	0.25	5.56	0.07	18	20.0
10	sextet 1	52.8	0.37	0.00	0.40	0.37	0.33	39	35.1
	sextet 2	51.2	0.30	0.03	0.52	0.84	0.30	143	56.2
	singlet		−1.33		0.23				0.6
	sextet 3	43.4	0.63	−0.65	0.25	7.90	0.21	31	8.1
0	sextet 1	51.1	0.30	0.00	0.42	0.77	0.69		35.5
	sextet 2	53.3	0.39	−0.01	0.56	0.15	0.69		56.7
	singlet		0.19		0.7				0.5
	sextet 3	47.1	0.92	−0.42	0.25	4.61	0.69		7.3

DOI: 10.1021/acs.jpcc.8b08988
J. Phys. Chem. C 2019, 123, 1444−1453

concerning the formation of the nanostructure, indicating the low solubility of the Zn ion in the AFM Wüstite phase (core), followed by the surface oxidation, leading to the formation of the FiM ferrite phase at the shell, keeping the Zn/Fe relation along the whole nanoparticle. The incorporation of Zn allows to modify the overall magnetic properties of the magnetic nanoparticles. The effective anisotropy of the shell decreases with an increase in the Zn amount; at the same time, the AFM ordering of the core leads to an increment in the anisotropy of the whole system below T_N. No significant change in the T_N of the AFM phase was observed with the limited incorporation of Zn. Finally, a strong magnetic coupling between both phases is evidenced by the presence of the exchange bias field, with a canting of the spins observed with an increase in the Zn amount in the system.

AUTHOR INFORMATION

Corresponding Author

*E-mail: lima@cab.cnea.gov.ar.

ORCID

Elin L. Winkler: 0000-0002-9575-7879

Enio Lima, Jr.: 0000-0002-6028-4274

Notes

The authors declare no competing financial interest.

ACKNOWLEDGMENTS

The authors are thankful to the Argentinian Agency ANPCyT for the financial support through the grants PICT 2016-0288, PICT 2015-0118, and PICT 2014-2612. This work was partially supported by FAPESP—Sao Paulo Research Foundation (Brazil, grant number 2016/21371-5). LCCMN is CNPq Fellows under grants 305.647/2015-6. The authors also acknowledge the European Community's financial support under the RISE H2020-MSCARISE-2016, SPICOLOST project.

REFERENCES

(1) Sun, S.; Zeng, H. Size-Controlled Synthesis of Magnetite Nanoparticles. *J. Am. Chem. Soc.* **2002**, *124*, 8204−8205.

(2) Sun, S.; Zeng, H.; Robinson, D. B.; Raoux, S.; Rice, P. M.; Wang, S. X.; Li, G. Monodisperse MFe2O4 (M = Fe, Co, Mn) Nanoparticles. *J. Am. Chem. Soc.* **2004**, *126*, 273−279.

(3) Park, J.; An, K.; Hwang, Y.; Park, J.-G.; Noh, H.-J.; Kim, J.-Y.; Park, J.-H.; Hwang, N.-M.; Hyeon, T. Ultra-large-scale Syntheses of Monodisperse Nanocrystals. *Nat. Mater.* **2004**, *3*, 891−895.

(4) Lee, Y.; Lee, J.; Bae, C. J.; Park, J.-G.; Noh, H.-J.; Park, J.-H.; Hyeon, T. Large-Scale Synthesis of Uniform and Crystalline Magnetite Nanoparticles Using Reverse Micelles as Nanoreactors under Reflux Conditions. *Adv. Funct. Mater.* **2005**, *15*, 503−509.

(5) Tavakoli, A.; Sohrabi, M.; Kargari, A. A Review of Methods for Synthesis of Nanostructured Metals with Emphasis on Iron Compounds. *Chem. Pap.* **2007**, *61*, 151−170.

(6) Kwon, S. G.; Hyeon, T. Formation Mechanisms of Uniform Nanocrystals via Hot-Injection and Heat-Up Methods. *Small* **2011**, *7*, 2685−2702.

(7) Frey, N. A.; Peng, S.; Cheng, K.; Sun, S. Magnetic Nanoparticles: Synthesis, Functionalization and Applications in Bioimaging and Magnetic Energy Storage. *Chem. Soc. Rev.* **2009**, *38*, 2532−2542.

(8) Roca, A. G.; Morales, M. P.; O'Grady, K.; Serna, C. J. Structural and Magnetic Properties of Uniform Magnetite Nanoparticles Prepared by High Temperature Decomposition of Organic Precursors. *J. Nanotechnol.* **2006**, *17*, 2783−2788.

(9) Roca, A. G.; Marco, J. F.; Morales, M. d. P.; Serna, C. J. Effect of Nature and Particle Size on Properties of Uniform Magnetite and Maghemite Nanoparticles. *J. Chem. Phys.* **2007**, *111*, 18577−18584.

(10) Vargas, J. M.; Zysler, R. D. Tailoring the Size in Colloidal Iron Oxide Magnetic Nanoparticles. *J. Nanotechnol.* **2005**, *16*, 1474−1476.

(11) Lima, E.; De Biasi, E.; Mansilla, M. V.; Saleta, M. E.; Effenberg, F.; Rossi, L. M.; Cohen, R.; Rechenberg, H. R.; Zysler, R. D. Surface Effects in the Magnetic Properties of Crystalline 3 nm Ferrite Nanoparticles Chemically Synthesized. *J. Appl. Phys.* **2010**, *108*, 103919.

(12) Arelaro, A. D.; Lima, E.; Rossi, L. M.; Kiyohara, P. K.; Rechenberg, H. R. Ion Dependence of Magnetic Anisotropy in MFe2O4 (M=Fe, Co, Mn) Nanoparticles Synthesized by High-temperature Reaction. *J. Magn. Magn. Mater.* **2008**, *320*, e335−e338.

(13) Hou, Y.; Xu, Z.; Sun, S. Controlled Synthesis and Chemical Conversions of FeO Nanoparticles. *Angew. Chem., Int. Ed.* **2007**, *46*, 6329−6332.

(14) McCammon, C. A. Magnetic properties of FexO (x > 0.95): Variation of Neel Temperature. *J. Magn. Magn. Mater.* **1992**, *104*−*107*, 1937−1938.

(15) Lak, A.; Cassani, M.; Mai, B. T.; Winckelmans, N.; Cabrera, D.; Sadrollahi, E.; Marras, S.; Remmer, H.; Fiorito, S.; Cremades-Jimeno, L.; et al. Fe2+ Deficiencies, FeO Sub-Domains, and Structural Defects Favor Magnetic Hyperthermia Performance of Iron Oxide Nanocubes into Intracellular Environment. *Nano Lett.* **2018**, *18*, 6856−6866.

(16) Khurshid, H.; Li, W.; Chandra, S.; Phan, M.-H.; Hadjipanayis, G. C.; Mukherjee, P.; Srikanth, H. Mechanism and Controlled Growth of Shape and Size Variant Core/Shell FeO/Fe_3O_4 Nanoparticles. *Nanoscale* **2013**, *5*, 7942−7952.

(17) Unni, M.; Uhl, A. M.; Savliwala, S.; Savitzky, B. H.; Dhavalikar, R.; Garraud, N.; Arnold, D. P.; Kourkoutis, L. F.; Andrew, J. S.; Rinaldi, C. Thermal Decomposition Synthesis of Iron Oxide Nanoparticles with Diminished Magnetic Dead Layer by Controlled Addition of Oxygen. *ACS Nano* **2017**, *11*, 2284−2303.

(18) Kamzin, A. S.; Valiullin, A. A.; Khurshid, H.; Nemati, Z.; Srikanth, H.; Phan, M. H. Mössbauer Studies of Core−Shell FeO/Fe3O4 Nanoparticles. *Phys. Solid State* **2018**, *60*, 382−389.

(19) Sharma, S. K.; Vargas, J. M.; Pirota, K. R.; Kumar, S.; Lee, C. G.; Knobel, M. Synthesis and Ageing Effect in FeO Nanoparticles: Transformation to Core−Shell FeO/Fe3O4 and their Magnetic Characterization. *J. Alloys Compd.* **2011**, *509*, 6414−6417.

(20) Chen, R.; Christiansen, M. G.; Sourakov, A.; Mohr, A.; Matsumoto, Y.; Okada, S.; Jasanoff, A.; Anikeeva, P. "High-Performance Ferrite Nanoparticles through Nonaqueous Redox Phase Tuning". *Nano Lett.* **2016**, *16*, 1345−1351.

(21) Vasilakaki, M.; Trohidou, K. N.; Nogués, J. Enhanced Magnetic Properties in Antiferromagnetic-Core/Ferrimagnetic-Shell Nanoparticles. *Sci. Rep.* **2015**, *5*, 9609.

(22) Lavorato, G.; Winkler, E.; Ghirri, A.; Lima, E.; Peddis, D.; Troiani, H. E.; Fiorani, D.; Agostinelli, E.; Rinaldi, D.; Zysler, R. D. Exchange Bias and Surface Effects in Bimagnetic CoO−Core/$Co_{0.5}Ni_{0.5}Fe_2O_4$-Shell Nanoparticles. *Phys. Rev. B: Condens. Matter Mater. Phys.* **2016**, *94*, 054432.

(23) Lavorato, G. C.; Lima, E.; Troiani, H. E.; Zysler, R. D.; Winkler, E. L. Tuning the Coercivity and Exchange Bias by Controlling the Interface Coupling in Bimagnetic Core/Shell Nanoparticles. *Nanoscale* **2017**, *9*, 10240−10247.

(24) Sun, X.; Huls, N. F.; Sigdel, A.; Sun, S. Tuning Exchange Bias in Core/Shell FeO/Fe3O4 Nanoparticles. *Nano Lett.* **2011**, *12*, 246−251.

(25) Kavich, D. W.; Dickerson, J. H.; Mahajan, S. V.; Hasan, S. A.; Park, J.-H. Exchange Bias of Singly Inverted FeO/Fe3O4 Core-Shell Nanocrystals. *Phys. Rev. B: Condens. Matter Mater. Phys.* **2008**, *78*, 174414.

(26) Leszczyński, B.; Hadjipanayis, G. C.; El-Gendy, A. A.; Załęski, K.; Sniadecki, Z.; Musiał, A.; Jarek, M.; Jurga, S.; Skumiel, A. The Influence of Oxidation Process on Exchange Bias in Egg-Shaped FeO/Fe3O4 Core/Shell Nanoparticles. *J. Magn. Magn. Mater.* **2016**, *416*, 269−274.

DOI: 10.1021/acs.jpcc.8b08988
J. Phys. Chem. C 2019, 123, 1444−1453

(27) Chen, C.-J.; Chiang, R.-K.; Kamali, S.; Wang, S.-L. Synthesis and Controllable Oxidation of Monodisperse Cobalt-Doped Wüstite Nanoparticles and Their Core−Shell Stability and Exchange-Bias Stabilization. *Nanoscale* **2015**, *7*, 14332−14343.
(28) Davar, F.; Salavati-Niasari, M.; Mir, N.; Saberyan, K.; Monemzadeh, M.; Ahmadi, E. Thermal Decomposition Route for Synthesis of Mn3O4 Nanoparticles in Presence of a Novel Precursor. *Polyhedron* **2010**, *29*, 1747−1753.
(29) Chen, Q.; Rondinone, A. J.; Chakoumakos, B. C.; Zhang, Z. J. Synthesis of Superparamagnetic MgFe2O4 Nanoparticles by Coprecipitation. *J. Magn. Magn. Mater.* **1999**, *194*, 1−7.
(30) Liu, C.; Zou, B.; Rondinone, A. J.; Zhang, Z. J. Chemical Control of Superparamagnetic Properties of Magnesium and Cobalt Spinel Ferrite Nanoparticles through Atomic Level Magnetic Couplings. *J. Am. Chem. Soc.* **2000**, *122*, 6263−6267.
(31) Carter, R. E. Thermal Expansion of MgFe,O, FeO, and MgO.2FeO. *J. Am. Ceram. Soc.* **1959**, *42*, 324−327.
(32) Hansson, R.; Hayes, P. C.; Jak, E. In Phase Equilibria in the Fe-Zn-O System at Conditions Relevant to Zinc Sintering and Smelting. In *Proceedings of VII International Conference on Molten Slags Fluxes and Salts*; The South African Institute of Mining and Metallurgy, 2004; p 209.
(33) Kmita, A.; Pribulova, A.; Holtzer, M.; Futas, P.; Roczniak, A. Use of Specific Properties of Zinc Ferrite in Innovative Technologies. *Arch. Metall. Mater.* **2016**, *61*, 2141−2146.
(34) Anooj, E. S.; Sreelekshmi, S. J.; Gopukumar, S. T.; Praseetha, P. K. Evaluation of the Zinc Ferrite Nano particles for Bio-applications. *Int. J. Pharm. Sci. Rev. Res.* **2017**, *46*, 22−26.
(35) Hanini, A.; Lartigue, L.; Gavard, J.; Kacem, K.; Wilhelm, C.; Gazeau, F.; Chau, F.; Ammar, S. Zinc Substituted Ferrite Nanoparticles with Zn0.9Fe2.1O4 Formula Used as Heating Agents for in vitro Hyperthermia Assay on Glioma cells. *J. Magn. Magn. Mater.* **2016**, *416*, 315−320.
(36) Yang, Y.; Liu, X.; Yang, Y.; Xiao, W.; Li, Z.; Xue, D.; Li, F.; Ding, J. Synthesis of Nonstoichiometric Zinc Ferrite Nanoparticles with Extraordinary Room Temperature Magnetism and Their Diverse Applications. *J. Mater. Chem. C* **2013**, *1*, 2875−2885.
(37) Johansson, S. A. E.; Campbell, J. L.; Malmqvist, K. G. *Particle-Induced X-ray Emission Spectrometry (PIXE)*; Wiley: Hoboken, USA, 1995.
(38) Limandri, S.; Olivares, C.; Rodriguez, L.; Bernardi, G.; Suárez, S. PIXE Facility at Centro Atomico Bariloche. *Nucl. Instrum. Methods Phys. Res., Sect. B* **2014**, *318*, 47−50.
(39) Campbell, J. L.; Boyd, N. I.; Grassi, N.; Bonnick, P.; Maxwell, J. A. The Guelph PIXE Software Package IV. *Nucl. Instrum. Methods Phys. Res., Sect. B* **2010**, *268*, 3356−3363.
(40) Lima, E.; Winkler, E. L.; Tobia, D.; Troiani, H. E.; Zysler, R. D.; Agostinelli, E.; Fiorani, D. Bimagnetic CoO Core/CoFe2O4 Shell Nanoparticles: Synthesis and Magnetic Properties. *Chem. Mater.* **2012**, *24*, 512−516.
(41) Dormann, J. L.; Fiorani, D.; Tronc, E. Magnetic Relaxation in Fine-Particle Systems. *Adv. Chem. Phys.* **1997**, *98*, 283−494.
(42) Smit, J.; Wijn, H. P. J. *Ferrites: Physical Properties of Ferrimagnetic Oxides in Relation to Their Technical Applications*; Philips Technical Library: Eindhoven, Netherland, 1959.
(43) Chinnasamy, C. N.; Narayanasamy, A.; Ponpandian, N.; Chattopadhyay, K.; Guérault, H.; Greneche, J.-M. Magnetic Properties of Nanostructured Ferrimagnetic Zinc Ferrite. *J. Phys.: Condens. Matter* **2000**, *12*, 7795−7805.
(44) Pandey, B.; Litterst, F. J.; Baggio-Saitovitch, E. M. Preferential Spin Canting in Nanosize Zinc Ferrite. *J. Magn. Magn. Mater.* **2015**, *385*, 412−417.
(45) Morrish, A. H.; Clark, P. E. High-Field Mossbauer Study of Manganese-Zinc Ferrites. *Phys. Rev. B: Solid State* **1975**, *11*, 278−286.
(46) Trohidou, K.; Vasilakak, M. Monte Carlo Studies of Magnetic Nanoparticles. In *Applications of Monte Carlo Method in Science and Engineering*; Mordechai, S., Ed.; IntechOpen, 2011; Chapter 20, pp 513−538.
(47) Estrader, M.; López-Ortega, A.; Golosovsky, I. V.; Estradé, S.; Roca, A. G.; Salazar-Alvarez, G.; López-Conesa, L.; Tobia, D.; Winkler, E.; Ardisson, J. D.; et al. Origin of the Large Dispersion of Magnetic Properties in Nanostructured Oxides: FexO/Fe3O4 Nanoparticles as a Case Study. *Nanoscale* **2015**, *7*, 3002−3015.
(48) Checherskaya, L. F.; Romanov, V. P.; Tatsienko, P. A. Mossbauer Effect in Wustite. *Phys. Status Solidi A* **1973**, *19*, K177−K182.
(49) Lima, E.; Brandl, A. L.; Arelaro, A. D.; Goya, G. F. Spin Disorder and Magnetic Anisotropy in Fe3O4 Nanoparticles. *J. Appl. Phys.* **2006**, *99*, 083908.
(50) Pianciola, B. N.; Lima, E.; Troiani, H. E.; Nagamine, L. C. C. M.; Cohen, R.; Zysler, R. D. Size and Surface Effects in the Magnetic Order of the CoFe2O4 Nanoparticles. *J. Magn. Magn. Mater.* **2015**, *377*, 44−51.

DOI: 10.1021/acs.jpcc.8b08988
J. Phys. Chem. C 2019, 123, 1444−1453